

## 4

# Experimental study of the drill string torsional vibrations

### 4.1

#### Introduction

An experimental apparatus of the drilling system is not easy to develop. Some papers illustrate test rigs with viscous and dry resistive torques, aiming to simulate the borehole conditions. Some relevant test rigs are described in [5, 14, 24, 25, 26]. This master dissertation proposes to develop a test rig in order to represent the torsional dynamical behavior of a drilling system in reduced scale and induce torsional vibrations by dry friction. Also, the stick-slip phenomenon may be observed in performed trials. *LabView* and *MatLab* softwares are used for data acquisition and post-processing, respectively.

Initially in this chapter, section 4.2 describes the test rig. The components, assemblies and materials used are detailed over this section. The characterization of the test rig is performed in section 4.3 with parameter estimations. The important parameters of the system are identified by an empirical method and nonlinear least-square technique in order to compare and ensure the proper parameter estimations. The calibration procedures of the force sensor are described in section 4.4.

Moreover, the numerical model of the test rig is also presented in this chapter. Section 4.5 reports the equations of motion which governs the behavior of the apparatus taking into account the electrical and mechanical proprieties held by the system. The results of the experimental apparatus are presented. Section 4.6 describes the bifurcation diagrams of the test rig, comparing with the numerical results.

Lastly, the conclusions of this chapter are summarized in section 4.7.

### 4.2

#### Description of the test rig

The test rig consists of a horizontal set-up composed by DC-motor, two rotors - one at the extremity position (rotor 1) and an other at the intermediate position (rotor 2). A low-stiffness shaft of steel is selected and a brake device is developed. Figure 4.1 illustrates the set-up of the test rig. In this dissertation, the rotor 2 is not attached. Thus, there is two inertias: rotor 1 and the mass moment of inertia

of the DC-motor. The DC-motor is connected to the low-stiffness shaft which is responsible for transmitting rotational motion to the rotors. These rotors rotate around their geometric center and the lateral motions are constrained by bearings (neglected). The DC-motor of the test rig is an *ENGEL GNM 5480-G6.1* of series *E*, as illustrated in Figure 4.2. This DC-motor presents a planetary gearbox which is responsible to provide a large torque output. The gearbox relation is 8:1 and, also, it has an internal PI controller. In this study, a PI control is implemented in the *Simulink* block diagram in order to provide sufficient motor torque. Thus, this gearbox relation was not considered into the equations of motion. This PI control is responsible to keep constant the angular velocity of the DC-motor  $MRPM$ . A schema of the test rig including the data acquisition, position of sensors, DC-motor and rotor 1 is illustrated in Figure 4.3.

The dry friction is imposed by a brake device at rotor 1 from a contact material in order to induce torsional vibrations. Figure 4.4 shows the device which imposes a contact force on the radial end of the brake disc creating a resistive torque to the rotary motion. The device is composed by the brake pads and disc. The brake disc is acceded to the rotor 1, which means that the rotor 1 and the disc keep the same angular speed over time. The brake pads are responsible for the contact with the brake disc, inducing dry friction.

The actuation for opening and closing the pads is driven by a analogue servo controller *Dual-BB CS-80 Giant Scale* from the *HOBBICO Command Servos*. The analogue servo is controlled by a pulse-width modulation technique in *Arduino Uno R3* board (see figure 4.5).



Figure 4.1: Test rig set-up.

In order to measure the speed at the rotor 1 and at the DC-motor, rotary encoders *LS Mecapion* (1000 ticks/revolution) are used (see Figure 4.6(a)). The friction torque on rotor 1 is measured by a force sensor SV50 R-5 from *Alpha Instrumentos* (Figure 4.6(b)) that it is mounted below the braking device (see Figure 4.4) so that the friction torque is measured by a reaction force of the rotor 1 on the brake pads (see Figure 4.4(a)). This reaction force is multiplied by the radius of the brake disc.

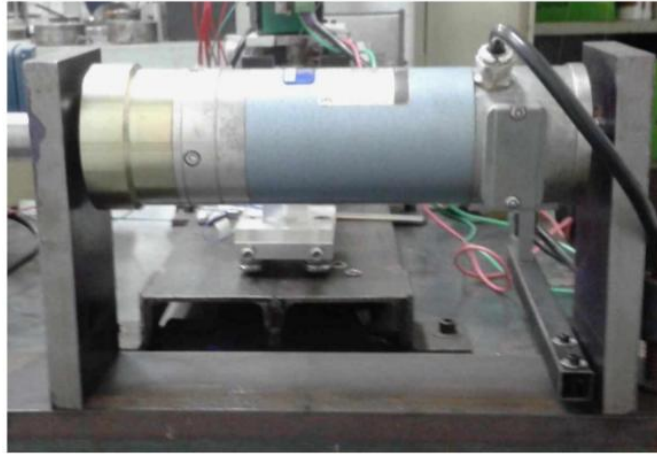


Figure 4.2: DC-motor of the test rig.

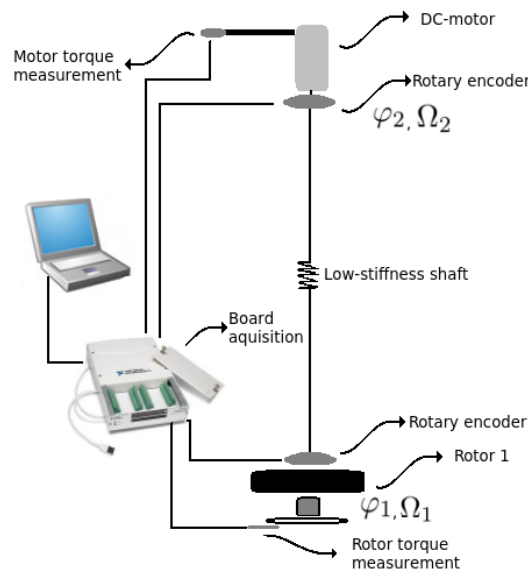


Figure 4.3: Test rig schema of measurements and positions.

The acquisition process is performed by the software *LabView 2010* and the acquired data are processed by software *MatLab*. Specifically, the data post-processing consists of a moving average in order to avoid noisy signal from the measuring environment with no significant signal loss. The acquisition board is NI USB-6229 of the *National Instruments* such as Figure 4.6(c) is shown.

The applied DC-motor torque is measured by a piezoelectric sensor PCB 208C01, shown in Figure 4.6(d). Indeed, the DC-motor applies torque and the system reacts on DC-motor with the same magnitude, therefore, the reactive torque from the system on motor is acquired. Figure 4.7 illustrates the developed schema to measure the torque from the motor.

Finally, all set-up values are presented in Table 4.1, representing the constants of the system.

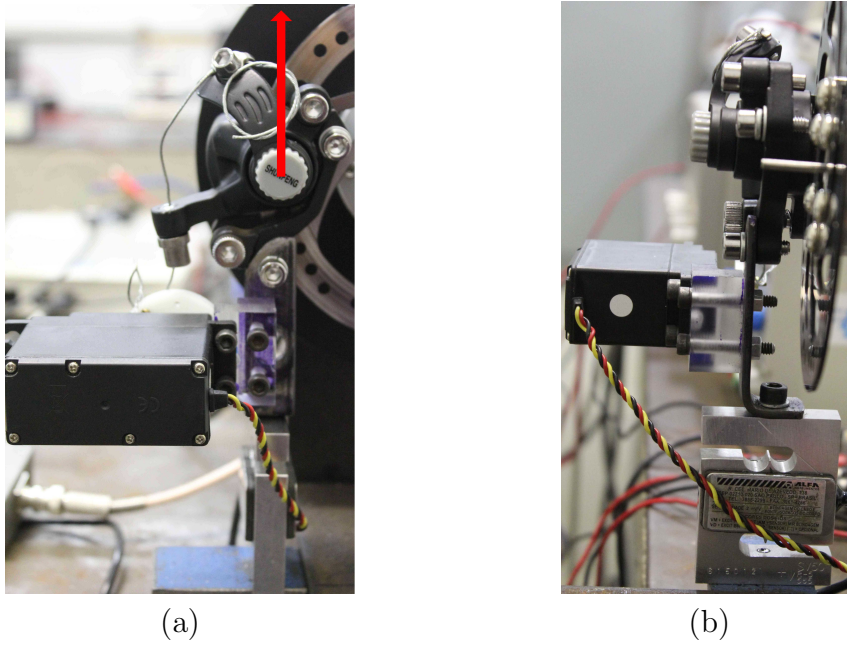


Figure 4.4: Brake device.



Figure 4.5: Arduino board.

Mechanical constants			
Parameter	Description	Value	Unit
$\rho_s$	String mass density	7850	$kg/m^3$
$L_s$	String length	2400	$mm$
$D_s$	Drill string diameter	3	$mm$
$E$	Young's modulus	210	$GPa$
$\nu$	Poisson ratio	0,30	—
$M_{r_1}$	Mass of the rotor 1	6,40	$kg$
$R_{r_1}$	Radius of the rotor 1	188	$mm$

Table 4.1: Mechanical parameter of test rig.

### 4.3 Parameter estimations

Before any test begins, it is important to characterize the test rig aiming to assure parameters values. The moment of inertia and stiffness of the system must be

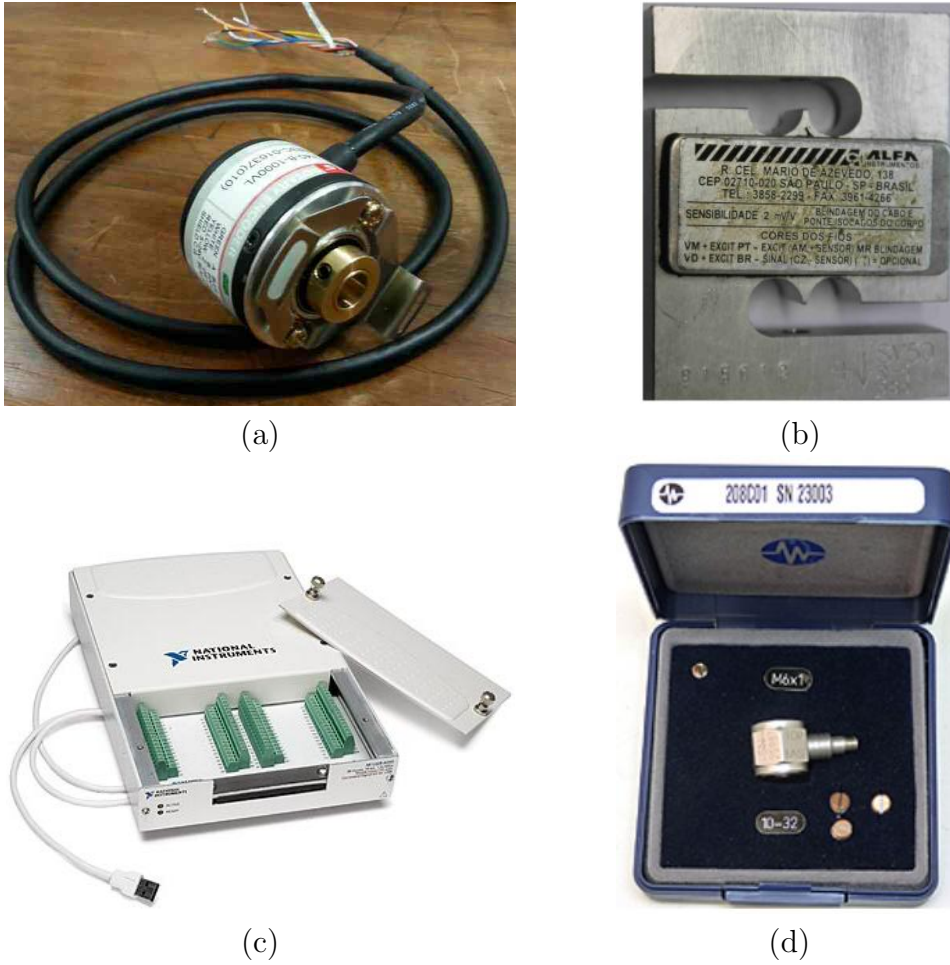


Figure 4.6: Measurement devices: (a) rotary encoder, (b) force sensor, (c) acquisition board, and (d) force sensor.

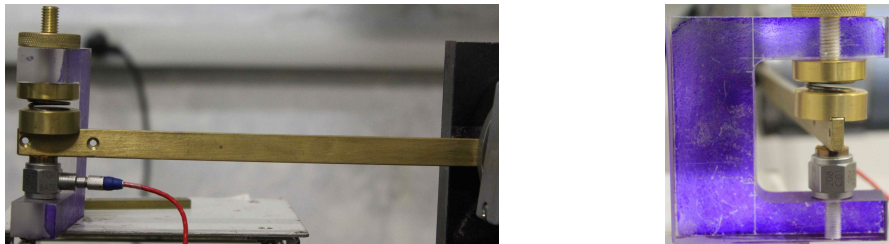


Figure 4.7: Schema to measure the applied reactive torque. (a) Front view and (b) lateral view.

estimated, thus, some trials are performed. Following, the characterization procedure of the experimental set-up is described and analyzed.

### 4.3.1 First estimation

At first, the stiffness of the low-string element ( $K_{s_A}$ ) is calculated analytically by Eq. 4-1 bellow,

$$K_{sA} = \frac{G I_s}{L_s} = 0.268 \text{ [Nm/rad]}, \quad (4-1)$$

where  $G$  is the shear modulus,  $I_s$  is the moment of inertia (geometric) and  $L_s$  is the length. As stated previously, the shear modulus  $G$  and the moment of inertia  $I_s$  may be achieved by  $G = \frac{E}{2(1+\nu)}$  and  $I_s = \frac{\pi}{32} D_s^4$ , respectively.  $D_s$  and  $\nu$  are the diameter of the shaft and the Poisson ratio. The used constants may be encountered in Table 4.1.

The natural frequency ( $\omega_n$ ) of the system with one DOF is acquired by applying input voltage of 8 V ( $\simeq 16 \text{ rad/s}$ ) of velocity at rotor 2. Clearly, the system includes unwanted points that are responsible for the loss of amplitude over time. It means that the damped frequency ( $\omega_d$ ) and period are obtained instead of the natural frequency and fundamental period. The approach by means Eqs. 4-2, the logarithmic decrement and the damping ratio are obtained, respectively, where  $x_1$  and  $x_2$  are successive amplitudes. Thus, Eq. 4-3 provides the  $\omega_n$ . Figure 4.8 illustrates the decay of the rotor speed as function of time. Table 4.2 presents the acquired and calculated values of the trials.

$$\delta = \ln \left( \frac{x_1}{x_2} \right), \quad (4-2a)$$

$$\xi = \frac{\delta}{\sqrt{(2\pi)^2 + \delta^2}}. \quad (4-2b)$$

$$\omega_n = \frac{\omega_d}{\sqrt{1 - \xi^2}}. \quad (4-3)$$

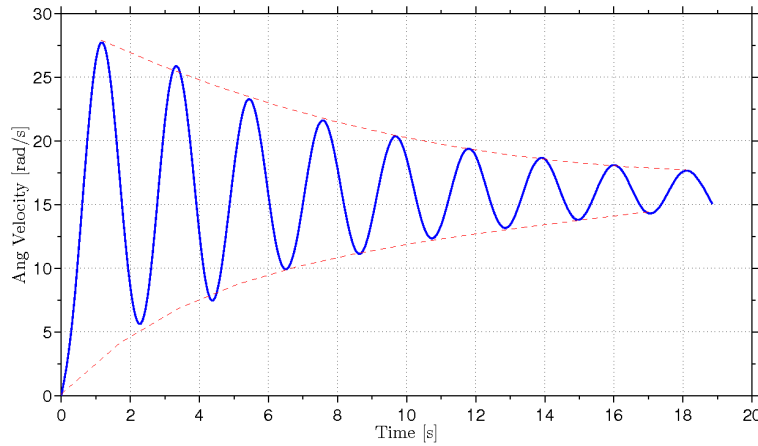


Figure 4.8: Time-domain response rotor 1 with input voltage of 8 V.

Therewith, the experimental moment of inertia of the rotor 1 ( $J_{1E}$ ) may be estimated by Eq. 4-4, using the mean of the measured natural frequency (Table 4.2) in [rad/s].

Trial	Peaks	Amplitude [rad]	$\delta$	$\xi$	$\omega_d$ [Hz]	$\omega_n$ [Hz]
1°	$x_1$	1.132	0.242	0.094	0.490	0.492
	$x_2$	0.889				
2°	$x_1$	1.026	0.253	0.098	0.485	0.488
	$x_2$	0.797				
3°	$x_1$	1.008	0.260	0.101	0.463	0.465
	$x_2$	0.777				
4°	$x_1$	1.100	0.255	0.099	0.483	0.486
	$x_2$	0.852				
<b>Mean</b>	$x_1$	1.067	0.253	0.098	0.483	0.485
	$x_2$	0.829				

Table 4.2: Experimental values of the test rig system.

$$\omega_n = \sqrt{\frac{K_{sA}}{J_{1E}}} \therefore J_{1E} = \frac{K_{sA}}{\omega_n^2} = 0.0287 [kg m^2]. \quad (4-4)$$

The mass of rotor 1 was obtained from its weight (Table 4.1) and the moment of inertia was analytically calculated by Eq. 4-5 bellow,

$$J_{1A} = \frac{1}{2} M_{r1} R_{r1}^2 = 0.0283 [kg m^2]. \quad (4-5)$$

The experimental and analytical values coincided, presenting 1.39 % of relative error.

For estimation of the stiffness to ensure the material proprieties of the string, the static test is performed. Figure 4.9 shows the used dynamometers to measure the applied force on rotor 1 and then the displacement is acquired by the rotary encoder. Table 4.3 contains the measured values of torque and displacement, and their respective stiffness of the string. In Figure 4.10 is shown the linear relation between torque and angular displacement for the verified values.



Figure 4.9: Used dynamometers of (a) 3B U20034 of 5 N (0.05 N of precision) and (b) Weiheng of 40 kg (0.01 kg of precision).

The relative error is calculated for analytical stiffness ( $K_{sA}$ ) and it does not reach large values which means that the characterization has been coincident, as the moment of inertia parameter analysis above (Table 4.3).

Trials	Torque [Nm]	Angle [rad]	$K_{SE}$ [Nm/rad]	Rel. Error [%]
1	0.142	0.556	0.255	4.879
2	0.139	0.532	0.260	2.877
3	0.277	1.104	0.251	6.331
4	0.305	1.181	0.259	3.447
5	0.315	1.217	0.267	0.494
<b>Mean</b>	-	-	0.258	3.606

Table 4.3: Experimental stiffness values and relative errors compared to analytical values.

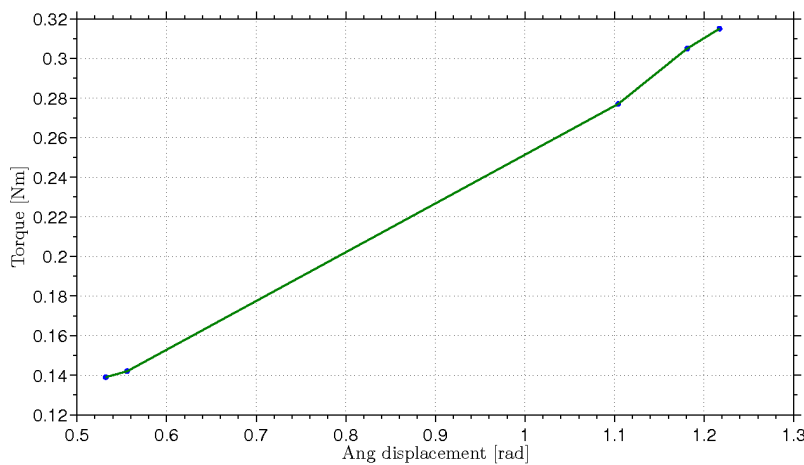


Figure 4.10: Relation between torque and angular displacement of the rotor 1.

### 4.3.2 Second estimation

Herein, the least-square technique is performed as a second estimation of all the system parameters, electrical and mechanical.

Firstly, due to uncertainties about few constants of the DC-motor and difficulty of find the exact corresponding operation manual (older model, no longer manufactured), an estimation is performed in order to ensure a best numerical representation of the test rig: the electrical parameters of the motor, the moment of inertia  $J_1$  and the stiffness  $K_s$ . Table 4.4 contains the initial values of the parameters to be estimated. The initial values of the DC-motor parameters were taken from a manual of a similar DC-motor and the analytical values of  $J_1$  and  $K_s$  were considered as initial values of the least-square technique.

Since the parameters of the test rig do not change as function of time, a constant input voltage is imposed. Then the data of displacements and rotations are acquired and the implemented numerical model of the experimental set-up is used. Figure 4.11 illustrates the test rig behavior (blue line) and the reconstructed behavior of the test rig (red line). In Figure 4.12 the misfit function (2-3) convergence

Parameter	Description	Value	Unit
$J_m$	Moment of inertia of the motor	$0.37 * 10^{-3}$	$kgm^2$
$L_{DC}$	Armature inductance	$1.10 * 10^{-3}$	$H$
$R_{DC}$	Armature resistance	0.33	$\Omega$
$k_T$	Torque constant	0.12	$Nm/A$
$k_e$	Voltage constant	$6.02 * 10^{-2}$	$V/(rad/s)$
$T_f$	Friction torque	0.1	$Nm$
$C_m$	Speed regulation constant	$1.91 * 10^{-4}$	$Nm/(rad/s)$
$J_1$	Moment of inertia of the rotor	0.0283	$kgm^2$
$K_s$	Stiffness	0.268	$Nm/rad$

Table 4.4: Initial values of the parameters.

by the number of iterations.

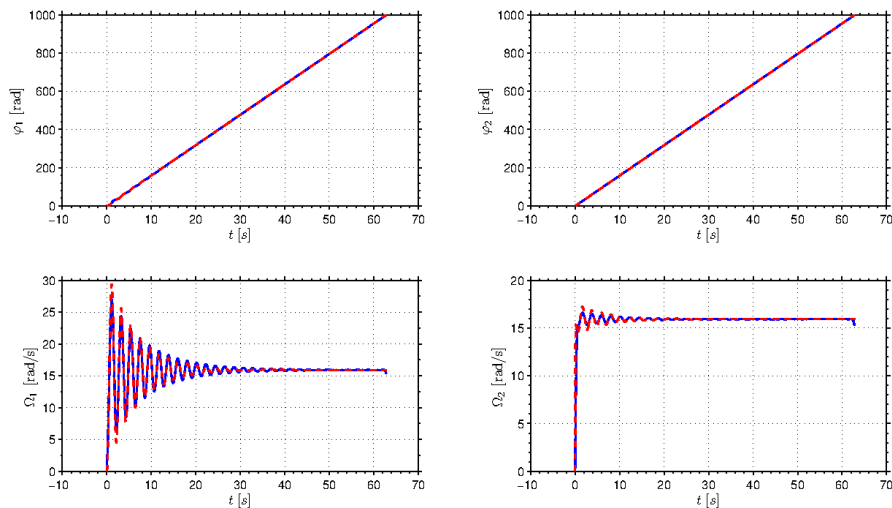


Figure 4.11: Response of the test rig (blue line) and estimation by least square (red line).

Therewith, the parameters are obtained and described in Table 4.5. Afterwards, these parameters will be used by the numerical model described in the following section.

#### 4.4 Calibration of the force sensors

In order to calibrate the force sensors, static trials are performed. For the sensor responsible for torque on motor illustrated in Figure 4.7, a torquimeter is used (see Figure 4.13). Known values of torque are imposed and the same values are reached from the sensor signal on *LabView* interface.

Likewise, known weights are used to calibrate the sensor mounted in brake device (see Figure 4.4). The same dynamometers of Figure 4.9 are used to measure

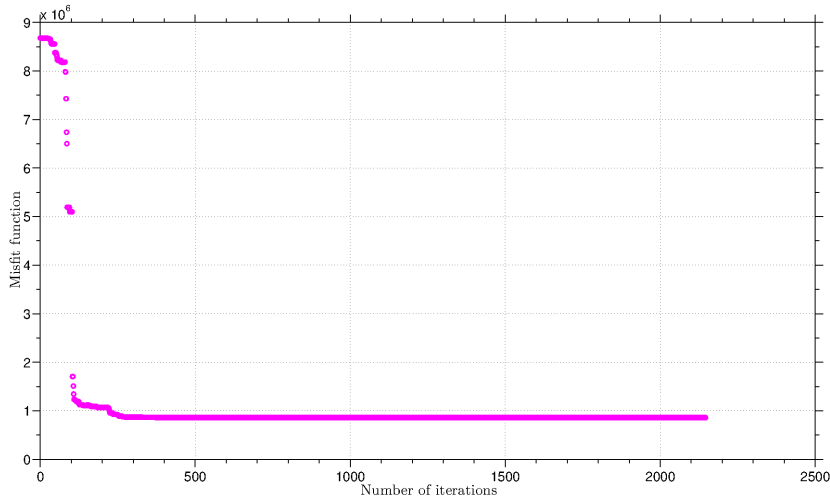


Figure 4.12: Convergence of the misfit function.

Parameter	Description	Value	Unit
$J_m$	Moment of inertia of the motor	$4.698 * 10^{-4}$	$kgm^2$
$L_{DC}$	Armature inductance	$8.437 * 10^{-4}$	$H$
$R_{DC}$	Armature resistance	0.526	$\Omega$
$k_T$	Torque constant	0.126	$Nm/A$
$k_e$	Voltage constant	0.0588	$V/(rad/s)$
$T_f$	Friction torque	0.1	$Nm$
$C_m$	Speed regulation constant	$1.784 * 10^{-4}$	$Nm/(rad/s)$
$J_1$	Moment of inertia of the rotor	0.0298	$kgm^2$
$K_s$	Stiffness	0.2710	$Nm/rad$

Table 4.5: Estimated values of the parameters.

the weights. Thus, voltage signals are acquired and a factor of conversion is encountered ( $Volts \rightarrow Newtons$ ), as Table 4.6 shows. Figure 4.14 illustrates the relation between voltage  $V$  and wights  $N$ .

Trials	Weight [N]	Voltage [mV]	Factor [mV/N]
1	0.758	161	212.401
2	3.704	798	215.443
3	3.754	804	214.171
4	5.484	1176	214.442
<b>Mean</b>	-	-	214.114

Table 4.6: Force sensor calibration.

With the purpose to ensure the calibration, the dynamometers are used once more. Several loads are imposed on the force sensor and the values given by the



Figure 4.13: Torquimeter device with 0.5 Nm of precision.

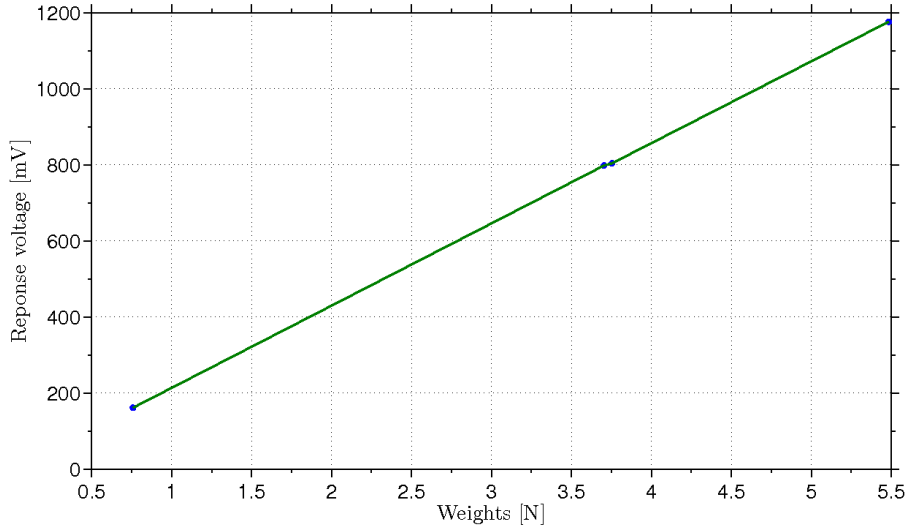


Figure 4.14: Voltage response as function of the weights.

sensor (in  $N$ ) must match with the imposed load values. With the mean value of Table 4.6, the imposed and measured values coincided.

#### 4.5 Mathematical modeling of the test rig

The numerical model of the test rig consists of two degrees of freedom - the rotor 1 and the inertia of the DC-motor. The equations of the DC-motor are included into modeling. The axial and lateral motions are constrained by the bearings.

The DC-motor equation is presented in Eq. 4-6 as follows

$$L \frac{di}{dt} + Ri + k_e \Omega_2 = V, \quad (4-6a)$$

$$T_m = k_T i - C_m \Omega_2 - T_f - J_m \dot{\Omega}_2, \quad (4-6b)$$

where  $i$  and  $T_m$  are the armature current and the motor torque, respectively.  $\Omega_3$  is the angular velocity of the inertia of the motor  $J_m$ .  $C_m$  and  $k_T$  are speed regulation and constant torque of the DC-motor, respectively. Further,  $k_e$  corresponds to the voltage constant,  $R$  and  $L$  are the armature resistance and inductance, respectively.

$T_f$  is an internal friction torque and  $V$  is the input voltage.

The two DOF's modeling is governed by Eq. 4-7, as follows. For convenience, the equations of motions are written in state-space form (Eq.4-8).

$$\begin{bmatrix} J_1 & 0 \\ 0 & J_m \end{bmatrix} \begin{bmatrix} \dot{\Omega}_1 \\ \dot{\Omega}_2 \end{bmatrix} + \begin{bmatrix} C & 0 \\ 0 & C_m \end{bmatrix} \begin{bmatrix} \Omega_1 \\ \Omega_2 \end{bmatrix} + \begin{bmatrix} k_1 & -k_1 \\ -k_1 & k_1 \end{bmatrix} \begin{bmatrix} \varphi_1 \\ \varphi_2 \end{bmatrix} = \begin{bmatrix} -T_1 \\ k_T i - T_f \end{bmatrix}, \quad (4-7)$$

$$\mathbf{q}' = \mathbf{A}\mathbf{q} + \mathbf{F}, \quad (4-8)$$

where  $\varphi_1, \varphi_2$  are the angular displacements of the rotor 1 and the inertia motor ( $J_m$ ), respectively.  $C$  is the damping of the test rig calculated by the damping parameter  $\xi$  (Eqs. 4-2 and Tab 4.2) and then  $C = 2 \cdot \xi \sqrt{J_1 \cdot k_1}$ .  $\Omega_1$  and  $\Omega_2$  are the angular velocities. The imposed dry friction torque to dissipate system energy is called  $T_1$ . In terms of state-space equations,  $\mathbf{A}$  is the matrix that contains the proprieties of the system (mechanical and electrical),  $\mathbf{F}$  is the vector with efforts and  $\mathbf{q}$  stands for state variables. Eq. 4-9 describes the variables of the first order system, the matrix  $\mathbf{A}$  and the efforts vector  $\mathbf{F}$ , as following,

$$\mathbf{q} = \begin{bmatrix} \varphi_1 \\ \varphi_2 \\ \Omega_1 \\ \Omega_2 \\ i \end{bmatrix}, \quad \mathbf{A} = \begin{bmatrix} 0 & 0 & 1 & 0 & 0 \\ 0 & 0 & 0 & 1 & 0 \\ -\mathbf{J}^{-1}\mathbf{K} & -\mathbf{J}^{-1}\mathbf{C} & 0 & 0 & 0 \\ 0 & 0 & 0 & -k_e/L & -R/L \end{bmatrix}, \quad \mathbf{F} = \begin{bmatrix} 0 \\ 0 \\ -T_1/J_1 \\ -T_f/J_m \\ V/L \end{bmatrix}. \quad (4-9)$$

As stated previously, the stick-slip is induced by dry friction imposed on rotor 1 ( $J_1$ ) while  $J_m$  continues rotating with constant speed. Numerically, the friction torque  $T_1$  is modeled as the modified Coulomb model as shown in section 3.3, i.e., the model presents difference between the static and dynamic coefficient,  $\mu_{st}$  and  $\mu_{dyn}$ , respectively. If the velocity of rotor 1 is lower than a stipulated tolerance ( $Tol = 0.001$ ) then the  $\mu_{st}$  is used, otherwise  $\mu_{dyn}$  is applied. The piecewise function of the  $T_1$  is represented in Eq. 4-10 while Figure 4.15 illustrates the used friction model.

$$T_1(\Omega_1) = \begin{cases} \mu_{st} \cdot N \cdot r & \text{if } \Omega_1 < Tol, \\ \mu_{dyn} \cdot N \cdot r & \text{if } \Omega_1 \geq Tol, \\ \mu_{neg} \cdot N \cdot r & \text{if } \Omega_1 < 0. \end{cases} \quad (4-10)$$

where  $N$  is the imposed normal force and  $r = 0.062 \text{ m}$  is the radius of the brake disc.  $Frict = \mu \cdot N$  and  $\mu$  can be  $\mu_{st}$ ,  $\mu_{dyn}$  or  $\mu_{neg}$ .  $\mu_{neg}$  is a "negative" friction coefficient if the angular velocity of the rotor 1 reaches negatives values. This is to maintain the friction torque as a dissipate torque even with negative speeds. Table

4.7 depicts the values of these coefficients and their set-points of RPM. These values were encountered by try-error comparing with the experimental results.

Coefficient	Description	Value	Set-points [RPM]
$\mu_{st}$	Static coefficient	1.60	0.05
$\mu_{dyn}$	Dynamic coefficient	1.20	0.50
$\mu_{neg}$	"Negative" coefficient	-0.20	$\leq 0$

Table 4.7: Friction coefficient and set-points values.

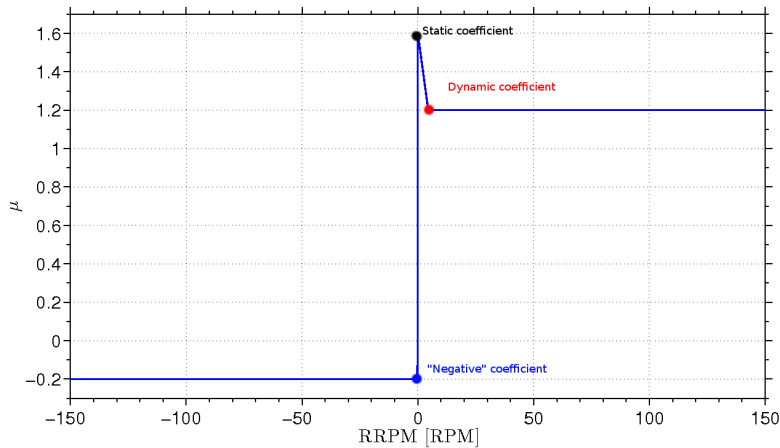


Figure 4.15: Modified Coulomb friction torque.

## 4.6 Results of the test rig model

The numerical and experimental torsional vibration maps are generated and compared in order to validate the model. Due to the difficulty to acquire several measuring points, only ten points were tested in order to construct the severity curve. In Figure 4.16 these maps are illustrated with friction at rotor 1  $F_{rict}$  and motor speed  $MRPM$ . Herein,  $RRPM$  denotes rotor speed.

Although the numerical curve does not present exactly the same points because the friction model adopted was not exactly encountered in the brake device. However, the behavior and the trend are the same as the experimental curve, presenting a qualitatively similar behavior. The numerical results of the test rig only present equilibrium and periodic solutions, as in the previous section. Figure 4.17(a) and 4.17(b) illustrated the periodic solutions in limit cycle of dimension one of the numerical model of the test rig.

The bifurcation diagrams of the numerical and experimental models are performed. As in previous chapter, the system passes from an equilibrium branch to a periodic branch, or vice versa. In order to create the bifurcation diagrams with  $MRPM$  as control parameter, the velocity of the motor is varied while the friction

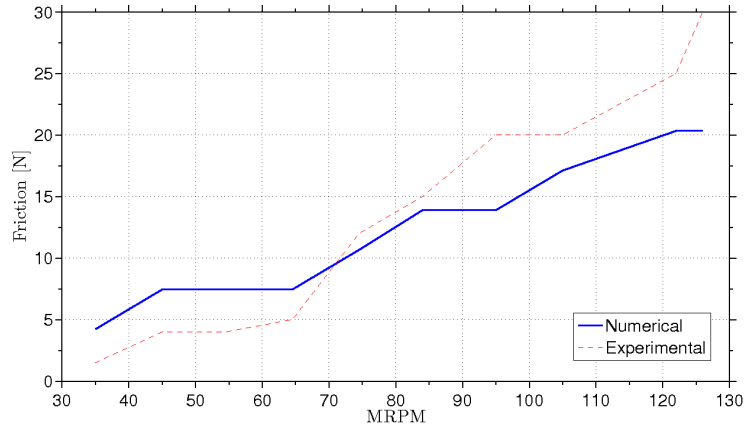


Figure 4.16: Numerical and experimental severity curves of the test rig.

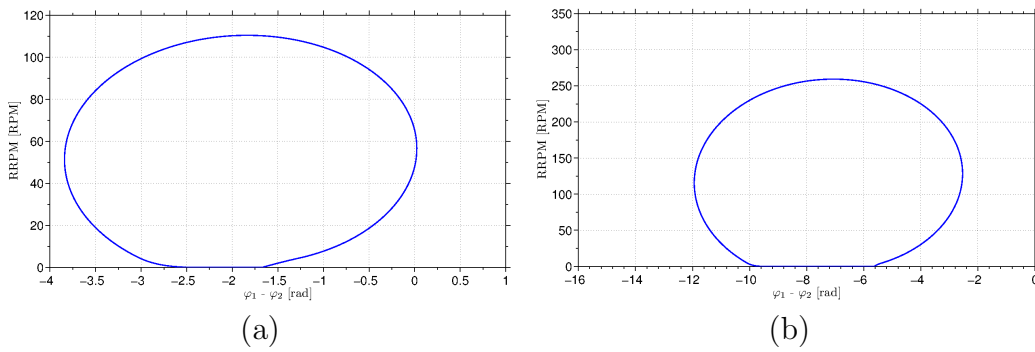


Figure 4.17: Limit cycles of the numerical model of the test rig: (a) 54.5 RPM and 4.5 N, and (b) 122 RPM and 25 N.

at the rotor 1 is kept constant. The maximum and minimum *RRPM* are acquired three times in each imposed motor speed and the average of these three results is recorded. This procedure was the same for the bifurcation diagrams with *Friction* as control parameter.

Figures 4.18(a) and 4.18(b) show the bifurcation diagrams for the motor speed *MRPM* as the control parameter, comparing experimental and numerical results, respectively. Experimentally, the time-domain response with and without torsional vibration is illustrated in Figure 4.19.

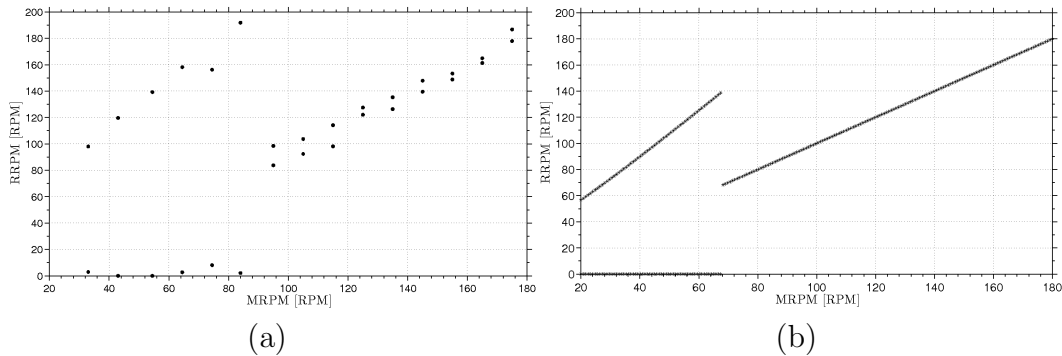


Figure 4.18: Bifurcation diagrams of the (a) experimental and (b) numerical models with 7.5 N constant.

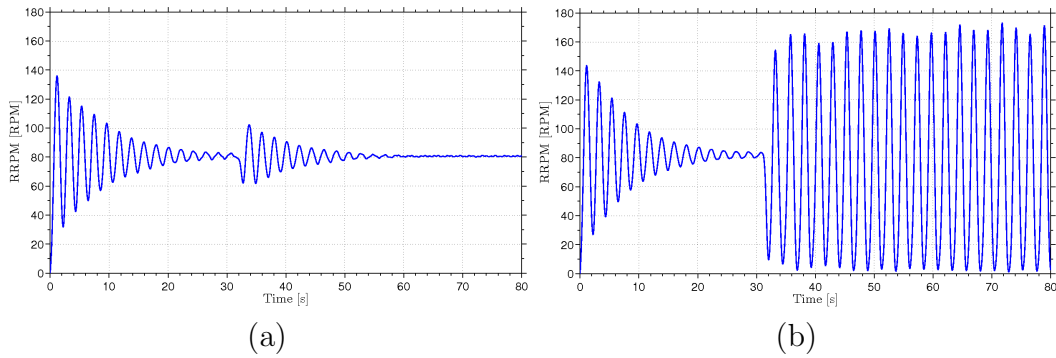


Figure 4.19: Experimental time-domain response with torsional vibration (a)  $Frict = 7.5\text{ N}$  and  $MRPM = 80\text{ RPM}$ , and without torsional vibration (b)  $Frict = 15\text{ N}$  and  $MRPM = 80\text{ RPM}$

Figures 4.20(a) and 4.20(b) illustrate the behavior when the friction is taken as control parameter. As noticed in the full scale model, the system behavior is more sensitive to friction effect as control parameter, where the  $Frict$  would be the  $DWOB$  of the previous section. Experimentally, the time-domain response with and without torsional vibration is depicted in Figure 4.21.

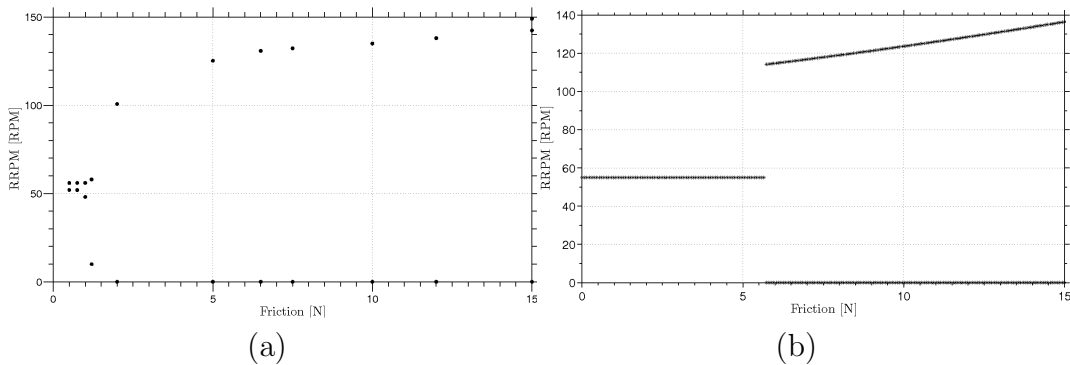


Figure 4.20: Bifurcation diagrams of the (a) experimental and (b) numerical models with 55 RPM constant.

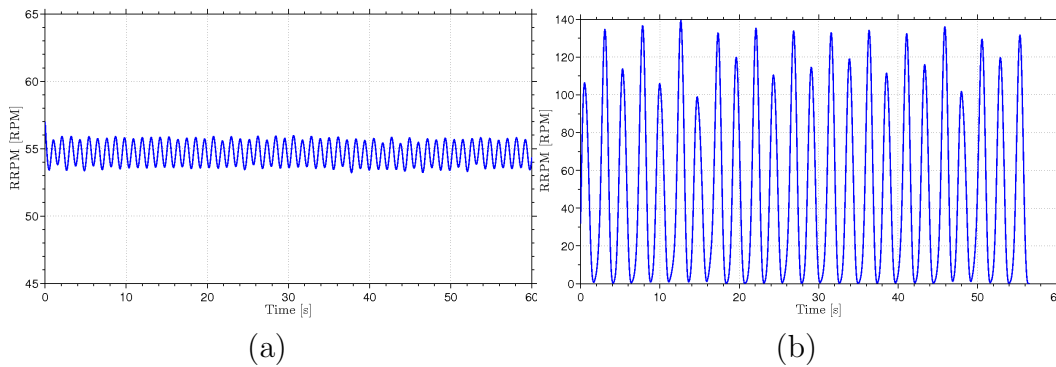


Figure 4.21: Experimental time-domain response with torsional vibration (a)  $Frict = 0.75\text{ N}$  and  $MRPM = 55\text{ RPM}$ , and without torsional vibration (b)  $Frict = 7.5\text{ N}$  and  $MRPM = 55\text{ RPM}$

The experimental limit cycles are observed in the test rig. As in the full scale model simulations, the system presents two stable solutions, but they are equilibrium points (without vibration) and quasi-periodic solutions (torsional oscillations). However, the system holds also quasi-periodic solutions. Figure 4.22 represents the limit cycle and time-domain response. The quasi-periodic solution is observed but not intensively apparent. In Figures 4.23 and 4.24 the quasi-periodic solution is more visible.

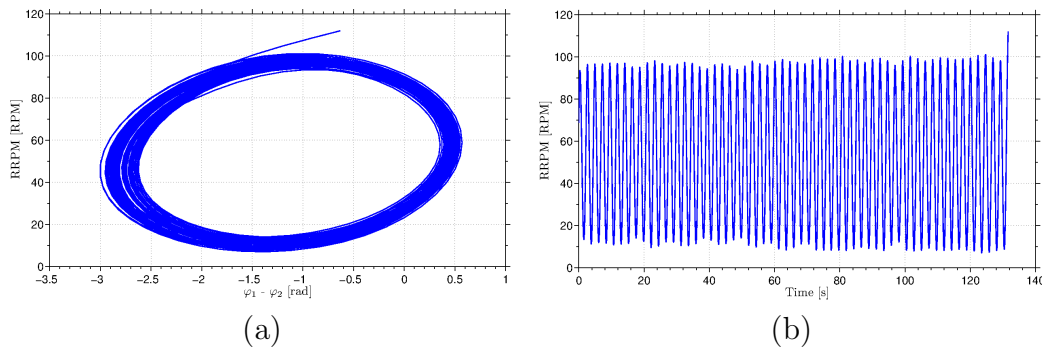


Figure 4.22: Test rig behavior with 54.4 RPM and 4.5 N of friction: (a) limit cycle, and (b) time-domain response.

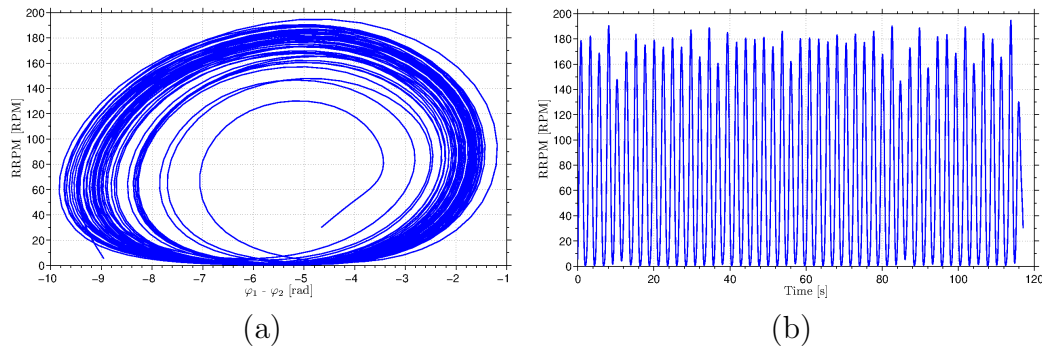


Figure 4.23: Test rig behavior with 84 RPM and 15 N of friction: (a) limit cycle, and (b) time-domain response.

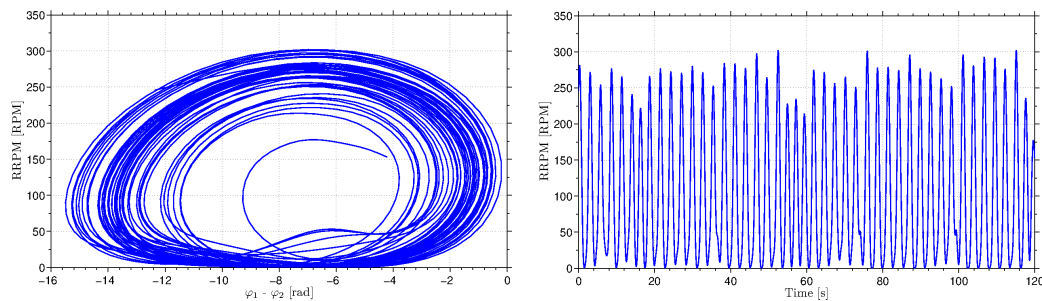


Figure 4.24: Test rig behavior with 122 RPM and 25 N of friction: (a) limit cycle, and (b) time-domain response.

The experimental system responses present frequency of oscillations around  $\simeq 0.4$  [Hz]. The numerical results present frequency around  $\simeq 0.3$  [Hz]. The rotor

$RPM$  reaches values between 300 and 0 RPM, as seen in Figure 4.24, and in Figure 4.17 the complete standstill of the rotor is observed, representing the stick-slip phenomenon. However, the negative rotor speed is not observed in both numerical and experimental results.

In order to investigate these quasi-periodic solutions, the frequency-response functions ( $FRF$ ) of the signals encountered in Figure 4.24 are performed. The angular velocity of the rotor 1 ( $RRPM$ ) and the torque on rotor 1 ( $RTor$ ) signals are used to perform the  $FRF$ 's. Although the brake device is mounted using a dry friction in the brake pads, the  $RTor$  present large oscillations. Figures 4.25 and 4.26 illustrate the time-domain response and  $FRF$ 's, respectively, of these measured data.

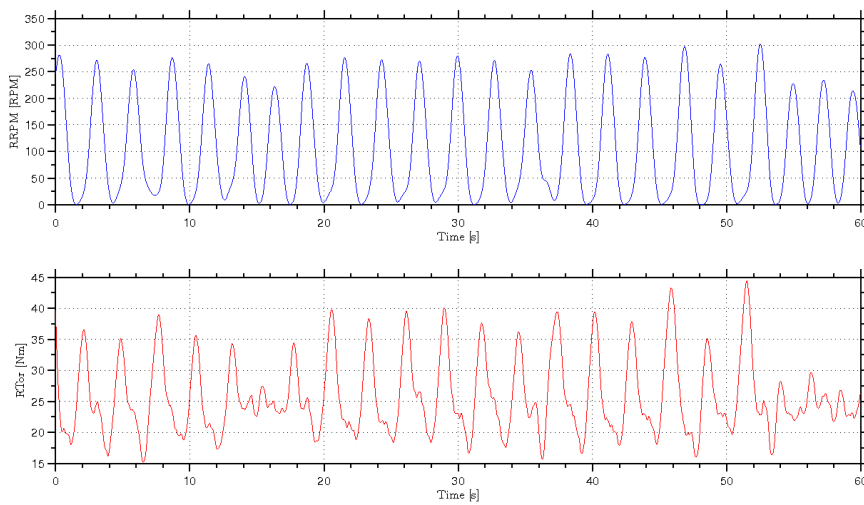


Figure 4.25: Time-domain response of the rotor angular velocity  $RRPM$  and torque on rotor 1  $RTor$ .

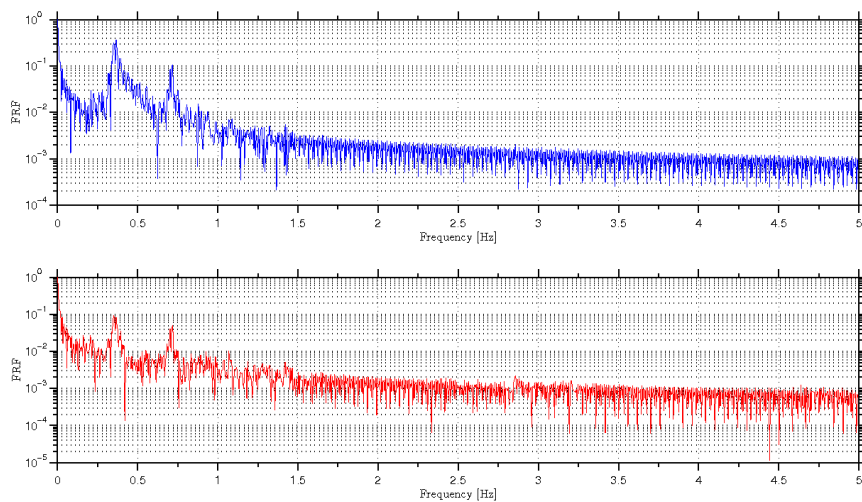


Figure 4.26: Frequency-response functions of the rotor angular velocity  $RRPM$  and torque on rotor 1  $RTor$ .

From Figure 4.26, three frequencies peak are registered and a sinusoidal signal with these frequencies is imposed in resistive torque model, i.e, Eq. 4-10 is modified as Eq. 4-11

$$T_1(\Omega_1) = \sin(\omega_p \cdot t) \cdot \begin{cases} \mu_{st} \cdot N \cdot r & \text{if } \Omega_1 < Tol, \\ \mu_{dyn} \cdot N \cdot r & \text{if } \Omega_1 \geq Tol, \\ \mu_{neg} \cdot N \cdot r & \text{if } \Omega_1 < 0, \end{cases} \quad (4-11)$$

where  $\omega_p$  is the frequency peak and  $t$  represents the time.  $\omega_p$  assumes the values shown in Table 4.8.

	Freq. peak [Hz]	Freq. peak [rad/s]
$\omega_p$	0.352	2.209
	0.718	4.510
	1.069	6.717

Table 4.8: Frequency peaks  $\omega_p$ .

Figures 4.27, 4.28, and 4.29 illustrate the time-domain responses and the limit cycles with the frequency peaks of the Table 4.8 above.

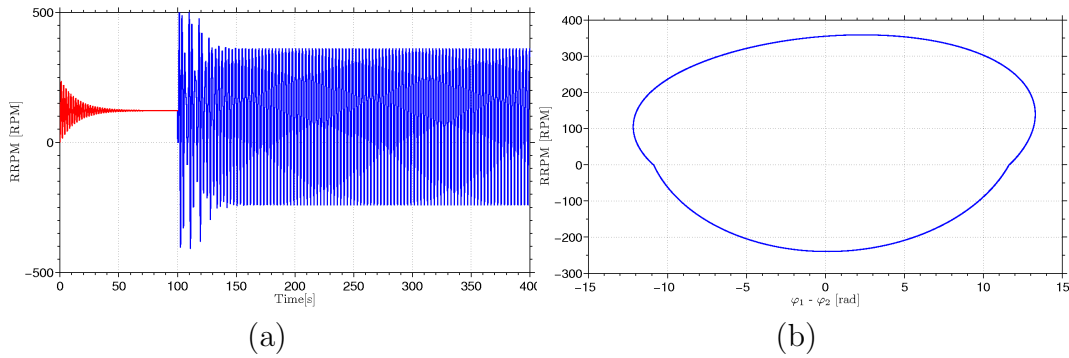


Figure 4.27: (a) Time-domain response, and (b) limit cycle of the test rig numerical model for  $Friect = 25$  N and  $MRPM = 122$  RPM with  $\omega_p = 2.209$  rad/s.

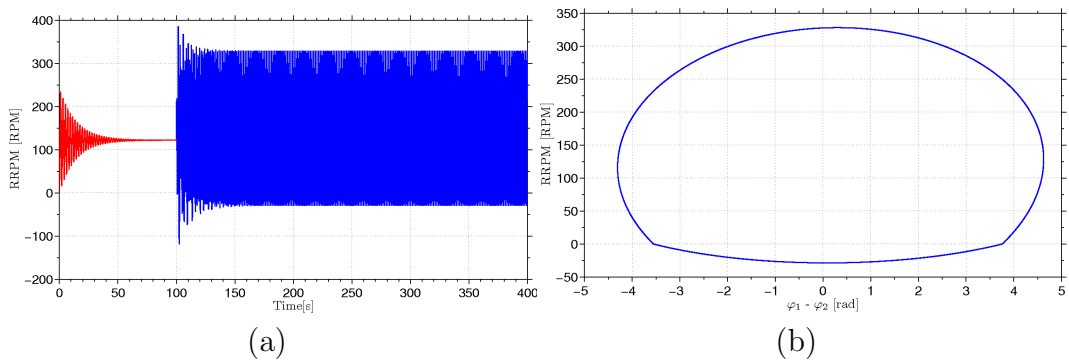


Figure 4.28: (a) Time-domain response, and (b) limit cycle of the test rig numerical model for  $Friect = 25$  N and  $MRPM = 122$  RPM with  $\omega_p = 4.510$  rad/s.

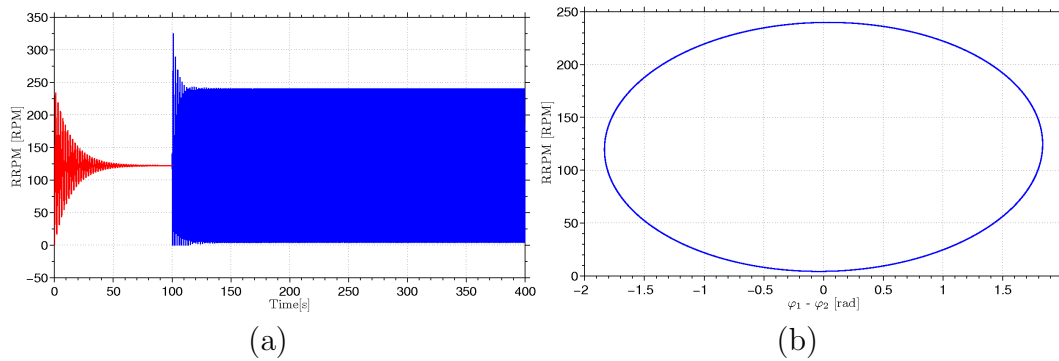


Figure 4.29: (a) Time-domain response, and (b) limit cycle of the test rig numerical model.  $F_{rict} = 25$  N and  $MRPM = 122$  RPM with  $\omega_p = 6.717$  Hz.

As it noticed, the inclusion of the sinusoidal function did create periodic solutions. Indeed, the effect of this harmonic function with frequency peaks decreases the vibration amplitudes and, consecutively, the displacement phases.

## 4.7

### Conclusion

The used instrumentation for data measurement and acquisition was described, as well as the post-processing method. The characterization of the test rig is of extreme importance before starting measurements described in this chapter.

The parameter estimation section presented two methods to identify parameters. First one was based on observation and data acquired of the experimental set-up. The amplitudes of the angular velocity oscillations were registered and the natural frequency was identified. Thus, mass moment of inertia of the rotor 1  $J_1$  was calculated assuming known stiffness. A second procedure was based on the maximization of the likelihood function (least-square technique). Due to uncertainties of the motor parameters, the least-square technique was also applied to these parameters. Initial values of all parameters (Table 4.4) are given and the convergence of the misfit function is observed. This procedure ensured the characterization and the estimated parameters values were afterwards used in the numerical model of the test rig.

Furthermore, the calibrations of the sensors were also described and the reliability of the measured data was ensured. All adopted test procedures were well detailed in this chapter.

The numerical model of the test rig was presented. The estimated parameters were used to construct the matrices of properties and the electrical parameters were included into the equations of motions. Also, the resistive torque induced by dry friction were described as a piecewise function differing static and dynamic torques. These  $\mu_{st}$  and  $\mu_{dyn}$  set-points were encountered by means comparing the test rig results.

Experimentally, dealing with dry friction is always a challenge. The stick-slip

induced by dry friction is observed in the experimental set-up. The numerical results of the test rig were presented, and comparisons between experimental and numerical results showed an interesting behavior. The test rig presented stick-slip and the limit cycles are depicted. However, the experimental test rig presented unexpected quasi-periodic solutions. During the measuring, the brake device vibrated when the pads were in contact with the brake disc. These vibrations possibly induced the appearance of other frequencies on the torsional response, characterizing the observed quasi-periodic solutions.

In order to identify and generate quasi-periodic solutions numerically, a sinusoidal function was implemented and the time domain responses and the limit cycles were depicted. Nevertheless, these results did not show quasi-periodic solutions. Rather, the results showed a decrease in the vibration amplitudes and displacement phases.

It is important remark that the torsional models did not present chaotic behavior.